Timing and magnitude of the Lomagundi–Jatuli carbon isotope excursion

Stacey Edmonsond[a,1] (ID) and Blake Dyer[a] (ID)

The rise of atmospheric oxygen during the Great Oxidation Event (GOE) (ca. 2.5 to 2.1 billion years ago) permanently transformed Earth's biogeochemical cycles. The chemistry of contemporaneous marine carbonates provides a window into operation of the carbon cycle across this transition. Specifically, carbonate rocks co-eval with the GOE preserve a large and long-lived positive carbon isotope (δ^{13}C) excursion, the Lomagundi–Jatuli excursion (LJE), that canonically is interpreted as an increase in organic matter burial linked to the oxygenation of Earth's surface. However, the cause, synchroneity, and global nature of the LJE remain contentious due to significant uncertainties in the excursion's timing and magnitude. These uncertainties stem from the incomplete, time-uncertain, and spatially variable nature of the shallow-water sedimentary record. Here, we use Bayesian inference to reconstruct Paleoproterozoic δ^{13}C from globally distributed stratigraphic observations. Our inference reaffirms that the LJE is a global excursion, although its expression varies locally, and provides revised estimates for its timing and magnitude. We find that δ^{13}C most likely began to increase at 2,445 Ma, subsequently returning to baseline values at 2,018 Ma. The most likely excursion peak occurs at 2,130 Ma, and it is very unlikely (5% probability) that peak δ^{13}C values exceeded 9.1‰. Altogether, our results indicate the LJE has an earlier onset, longer duration, and lower magnitude than previously thought. The initial δ^{13}C increase occurs before or contemporaneously with both the earliest rise of atmospheric O_2 and Paleoproterozoic "snowball" glaciations, hinting at a mechanistic link among the LJE, the GOE, and climate.

Lomagundi excursion | Great Oxidation Event | carbon cycle | geochemistry | stratigraphy

A conspicuous and enduring transition from mass-independent to mass-dependent fractionation of rock-bound sulfur isotopes marks the initial oxygenation of Earth's atmosphere around 2.5 to 2.1 billion years ago (1, 2). This redox transformation, termed the Great Oxidation Event (GOE; 3), is broadly coincident with global glaciations, the proliferation of oxygenic photosynthesis, and the emergence of continental landmasses (4–7). Rocks coeval with the GOE also preserve a large positive excursion in the carbon isotopic composition (δ^{13}C) of carbonate rocks (the Lomagundi–Jatuli excursion, or LJE; 8), pointing toward sustained (at least 130 Myr duration; 9) upheaval of global biogeochemical cycles. Canonically, the LJE has been interpreted as a prolonged episode of increased organic matter burial that facilitated the buildup of atmospheric O_2 (8, 10). However, the large apparent magnitude of the excursion (observed δ^{13}C values as high as 17 to 28‰; 11, 12) is difficult to reconcile with both carbon cycle mass balance requirements and a paucity of contemporaneous organic-rich rocks (11, 13, 14), leading some workers to posit that elevated Paleoproterozoic δ^{13}C values reflect local environmental conditions rather than global seawater $\delta^{13}C_{DIC}$ (11, 15–17). Other alternative models for the LJE maintain that it tracks global $\delta^{13}C_{DIC}$, but attribute the excursion to changes in the size and δ^{13}C of carbon input fluxes (18–21) or authigenic carbon reservoirs (22–24). Thus, the excursion's cause and connection to the GOE remain contentious.

Much of the discourse surrounding the LJE stems from large uncertainties in its timing, rate, and magnitude (25). For example, due to poor age control it is unclear whether the LJE represents a synchronous global excursion, asynchronous local excursions, or some intermediary (i.e., a global signal whose expression is modulated by local depositional environment) (11, 16, 17). In addition, the loosely constrained temporal relationship between the LJE and the GOE blurs potential causal relationships, hindering distinction between competing models for both events (10, 14, 20, 21, 26–29). The magnitude of the LJE also serves as a litmus test for different models, but current estimates—ranging from approximately 8 to 16‰ (30–32)—have limited discriminatory power. Elucidating

Significance

The rise of atmospheric oxygen during the Great Oxidation Event (GOE) set the stage for the evolution of complex life. Co-eval marine carbonate sediments preserve a large and long-lived positive carbon isotope (δ^{13}C) excursion, the Lomagundi–Jatuli excursion (LJE), that suggests this redox transformation was accompanied by a major carbon cycle perturbation. However, the timing, magnitude, and global extent of the LJE are uncertain due to the incomplete nature of the sedimentary record. Consequently, the excursion's cause and relationship to the GOE are debated. Here, we use statistical modeling to reconstruct the LJE from a global data compilation. Our results suggest the LJE has a lower magnitude and earlier onset than previously thought, strengthening its temporal correlation with Earth's oxygenation.

Author affiliations: [a]School of Earth and Ocean Sciences, University of Victoria, Victoria, BC V8P 5C2, Canada

the structure, timing, and nature of the LJE thus is essential for understanding both the carbon and oxygen biogeochemical cycles across a critical juncture in Earth's evolution.

The structure and timing of the LJE are uncertain owing to three fundamental features of the Paleoproterozoic sedimentary record. First, the majority of preserved Precambrian sediments come from marginal shallow-water depositional environments. These shallow-water strata are incomplete and punctuated by hiatuses [33], leading to poor signal preservation and complex relationships between stratigraphic height and time. Second, absolute age constraints (e.g., radiometrically dated ash beds and detrital minerals) are sparse, particularly within shallow-water carbonate sequences that host the LJE. Third, carbonate δ^{13}C can be influenced by local syndepositional processes (e.g., biological activity in restricted waters) and altered during diagenesis, partly decoupling preserved δ^{13}C values from that of global seawater $\delta^{13}C_{DIC}$ at the time of deposition [34]. Observed δ^{13}C heterogeneity within and among basins suggests many Paleoproterozoic carbonates have been affected by one or both of these processes [17, 25]. Together, these three features obfuscate the true structure of the LJE: Given its long duration, piecing together the full excursion requires merging highly fragmentary, time-uncertain, and locally biased observations from many different locations.

Previous reconstructions of the LJE rely on visual correlation of δ^{13}C profiles among basins; where available, correlation is guided by geochronological ages and sequence stratigraphic interpretations. Due to the fragmentary and locally variable nature of the observations, this manual approach yields poorly reproducible reconstructions of δ^{13}C over time: Different authors considering the same data have proposed a wide range of excursion magnitudes and durations, and the excursion's rising and falling limbs are particularly poorly resolved [30–32]. Furthermore, manual reconstructions may be biased toward sections that, although particularly well-studied or putatively complete, may not faithfully track global seawater chemistry. For example, some workers posit that the magnitude of the LJE has been overestimated because reconstructions are biased toward restricted shallow-water environments with locally elevated δ^{13}C values [17]. Reconstructions of the LJE's falling limb, for instance, are based largely on sections in Gabon and Fennoscandia that preserve a decline in δ^{13}C from peak values of 9 to 19‰ to baseline values near 0‰. However, δ^{13}C and depositional environment are strongly correlated in both of these basins [16, 17], evoking concern that stratigraphic trends in δ^{13}C may track the evolution of local environmental conditions rather than global $\delta^{13}C_{DIC}$. Recent geochronology also indicates the Fennoscandian succession may actually postdate the LJE [35], further calling the global nature of preserved δ^{13}C values into question.

Constraining the true timing and magnitude of the LJE calls for a more explicit and reproducible approach to reconstructing past changes in global δ^{13}C from the sedimentary record. To accomplish this, we developed a Bayesian statistical framework for determining the global δ^{13}C history that can best explain a given set of stratigraphic observations [36]. Our model simultaneously correlates all stratigraphic sections, constructs an age model for each section, decomposes global and local geochemical signals, and quantifies uncertainty in all parameters. Here, we use this model to reconstruct Paleoproterozoic δ^{13}C from globally distributed stratigraphic data. Our probabilistic reconstruction of δ^{13}C yields revised estimates for the timing and magnitude of the LJE, constrains the global versus local nature of the excursion, and elucidates its temporal relationship with Earth's Great Oxidation.

Bayesian Inference Model

Bayesian modeling allows us to merge geologic principles with quantitative data to make inferences about past Earth system change. Our model, StratMC (*Materials and Methods*, ref. 36), reconstructs past large-scale changes in seawater δ^{13}C from stratigraphic δ^{13}C observations and geochronological age constraints. The model is built around two simple assumptions: that depositional age decreases with stratigraphic height (superposition) and that there is a shared component to the δ^{13}C signal recorded by all stratigraphic sections. We refer to this shared component as the "global signal." The shape and timing of the global signal is learned from the data via Gaussian process regression. Within each section, local variations in δ^{13}C are incorporated via an offset term, which captures constant shifts relative to the global signal, and a geologic noise term, which accounts for any residual deviations. These per-section offset and noise terms are learned directly from the data. Since marginal shallow-water strata can have complex and irregular depositional histories, the prior age model for each section encompasses the full range of geologically reasonable sedimentation rates (i.e., depositional histories ranging from constant to highly episodic).

Importantly, the model does not assume a priori that a global excursion exists. Instead, the global signal may assume a wide range of functional forms to reflect evidence in the data. A δ^{13}C excursion will only be inferred if it is preserved by multiple stratigraphic sections. If the input sections do not preserve a common δ^{13}C trend, then the inferred global signal will be flat (e.g., a constant value of 0‰).

Paleoproterozoic Data Compilation

Our Paleoproterozoic δ^{13}C database (modified from ref. 25) includes 7,959 observations distributed across six continents and 120 geologic formations. This comprehensive dataset must be subsampled prior to running the model because the computational expense of our fully Bayesian inversion approach precludes using more than several hundred δ^{13}C observations. Our subsampling methodology ensures complete geographic and temporal coverage, preserving the stratigraphic δ^{13}C trend recorded in each basin while filtering redundant observations and noise (*Materials and Methods*). The subsampled dataset includes a representative subset of 849 δ^{13}C observations from 110 formations (Fig. 1*A*).

Based on the primary sources' interpretations of the sedimentology, the depositional environment of each sample is classified as deep-water (lower ramp to deep basin), intermediate (mid-upper ramp to platform), or shallow-water (sabkha to peritidal) (following the classification scheme of ref. 25). The subsampled dataset includes 134 deep-water, 405 intermediate, and 270 shallow-water samples; an additional 40 samples come from unknown depositional environments.

The age of each section in the δ^{13}C database is constrained by published geochronological data. Reported geochronological ages largely come from U-Pb system dating of both igneous and detrital zircon grains, but also include Pb-Pb dates for whole-rock carbonate samples and Re-Os dates for gabbro, peridotite, and early diagenetic pyrite. The age constraints used for each region are detailed in *SI Appendix*; example data for the Pechenga Greenstone Belt are in Fig. 1*B*.
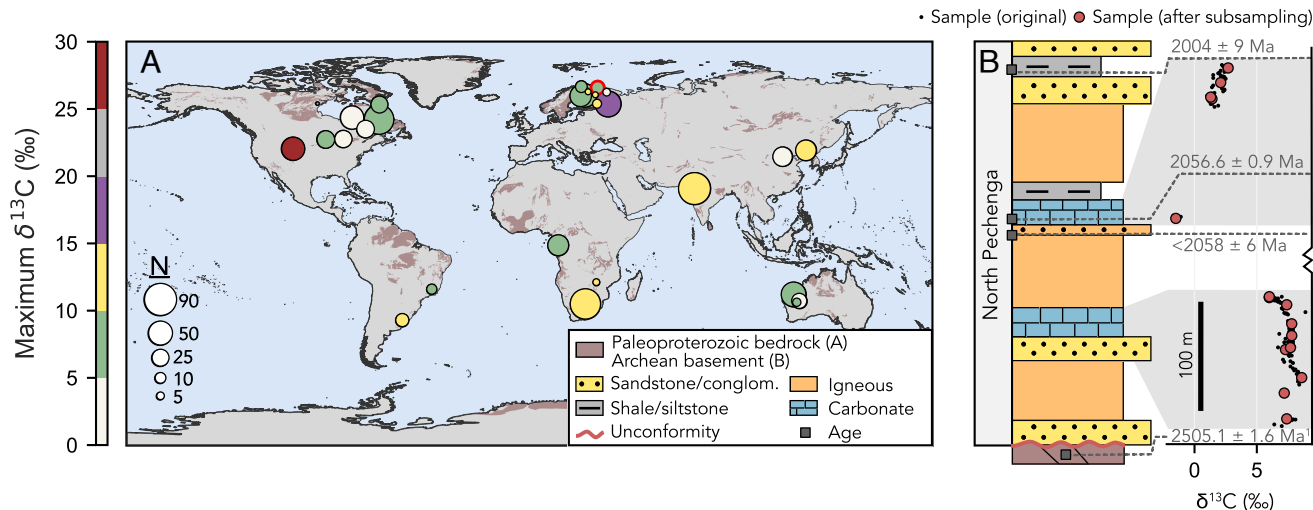
Fig. 1. Modern geographic distribution of Paleoproterozoic δ^{13}C observations and example stratigraphic data. (*A*) Locations of sections included in the Paleoproterozoic δ^{13}C inference (priority levels 1 and 2; *SI Appendix*). Each marker represents a unique supergroup (or group, where formations are not assigned to a supergroup). Marker size is scaled by the total number of δ^{13}C observations associated with the supergroup after subsampling (*SI Appendix*, Fig. S1 shows sample counts prior to subsampling), and marker color tracks the maximum observed δ^{13}C value. Paleoproterozoic bedrock coverage is from the Macrostrat database (37). (*B*) Generalized lithostratigraphy (modified after 38–40), δ^{13}C chemostratigraphy (38, 41), and geochronological age constraints (39, 40, 42) for the lower Pechenga Greenstone Belt in the Kola Craton, Russia. Location of the Pechenga Greenstone Belt is outlined in red in (*A*). Stratigraphy for all basins is in *SI Appendix*, Figs. S4–S36.

To interrogate the relationship between the LJE and atmospheric oxygenation, we also catalog multiple sulfur isotope data from basins included in the δ^{13}C inference (data compiled by refs. 43 and 44). Each geologic unit is classified as preserving mass-independent (MIF-S), mass-dependent (MDF-S), or mixed (i.e., MDF-S with restricted occurrences of MIF-S, or vice-versa) sulfur isotope fractionation.

Results and Discussion

Reconstructing Paleoproterozoic δ^{13}C. Our inference results reaffirm that the Paleoproterozoic δ^{13}C observations can be explained by a high-magnitude and long-duration positive excursion (Fig. 2*A*). Specifically, δ^{13}C began increasing from baseline values as early as 2,507 Ma (5% probability), with this increase very likely (95% probability) occurring before 2,276 Ma. It is likely ($\geq$66% probability) that δ^{13}C values exceeded 2‰ from 2,368 until 2,042 Ma. The maximum δ^{13}C value achieved during the excursion is very unlikely (5% probability) to have exceeded 9.1‰, and the excursion peak very likely (95% probability) occurs before 2,110 Ma. Following this peak, δ^{13}C returns to baseline values as early as 2,038 Ma (5% probability), with the excursion very likely (95% probability) terminating by 1,865 Ma. The total duration of the excursion very likely (95% probability) exceeds 253 Myr and is very unlikely (5% probability) to exceed 585 Myr.

Altogether, the most likely scenario is that δ^{13}C began to rise at 2,445 Ma, reaching a peak value of 7.3‰ at 2,130 Ma before returning to baseline values at 2,018 Ma. The most likely excursion duration is 429 Myr (Table 1).

Defining the LJE. Before comparing our inference with previous reconstructions of the LJE, careful calibration of terminology is required. While the LJE universally is considered to be a high-amplitude and long-duration positive δ^{13}C excursion centered around 2.2 Ga, its precise definition is not standardized. For example, Martin et al. (9) consider that carbonate rocks with

δ^{13}C above 5‰ represent the LJE, while Bekker (32) places baseline δ^{13}C during the LJE near 8‰ and considers pre-2.22 Ga carbonate rocks with less positive δ^{13}C values to be precursors to the main excursion. These threshold-based definitions are optimized for manually constructed δ^{13}C curves, which tend to be somewhat stylized due to the piecemeal nature of the data.

Our continuous δ^{13}C inference facilitates more nuanced description of the LJE's timing and structure. In particular, our approach enables more precise resolution of the excursion's onset and termination, which aids in constraining its cause. We consider that the LJE began when δ^{13}C first started to rise toward peak values (with no intervening return to pre-excursion baseline values below 2‰) and ended when δ^{13}C subsequently declined and restabilized. Probabilities are used to quantify excursion intensity between these endpoints. We note that under this definition, the excursion's rising limb is not required to increase monotonically; in some posterior realizations, the overall δ^{13}C rise is punctuated by "plateaus" or negative oscillations (while remaining above 2‰). Although we acknowledge that no simple definition can perfectly describe the full range of posterior excursion structures, we believe these criteria accurately capture the period of time when δ^{13}C values are persistently perturbed.

A Revised View of the LJE. Three aspects of our Paleoproterozoic δ^{13}C curve deviate notably from previous reconstructions. First, the likely magnitude of the LJE is lower than previously thought: The upper bound of our peak δ^{13}C estimate is similar to the lower bound of most other estimates, while our most likely peak is around 2‰ lower (Table 1). This more subdued excursion is the common (global) signal that is shared among all stratigraphic sections. Any local departures from this common signal—for example, extremely elevated δ^{13}C values preserved in some stratigraphic sections—are most parsimoniously explained as nonglobal processes occurring within individual basins or depositional environments.

Second, our inference reveals that δ^{13}C likely began to rise approximately 75 to 250 Myr earlier than the typically reported
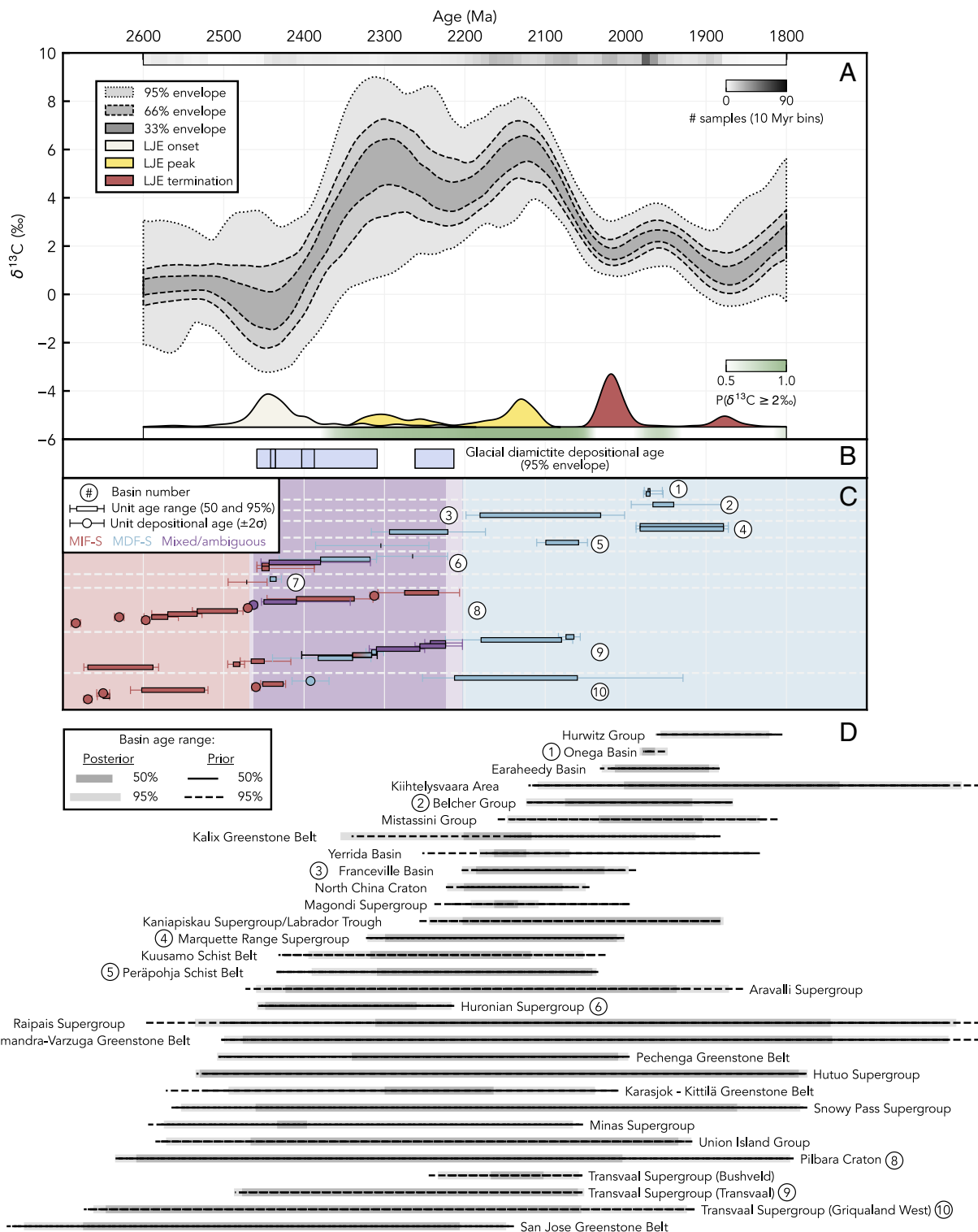
Fig. 2. Summary of Paleoproterozoic inference results. (*A*) δ^{13}C history inferred using 849 carbonate δ^{13}C observations and 124 age constraints from 110 different formations. The *Upper* colorbar shows posterior observation density (in 10 Myr bins) while the *Lower* colorbar tracks the probability that the inferred δ^{13}C signal exceeds 2‰. Relative probability densities for the timing of the LJE onset, peak, and termination are plotted along the *Lower* x-axis. (*B*) Depositional age ranges for glacial diamictites associated with four purported Paleoproterozoic glacial intervals. Age ranges reflect the maximum and minimum possible age for each glacial interval considering all geochronological ages, posterior age models, and plausible correlations among basins (*SI Appendix*). (*C*) Compiled observations of mass-independent and mass-dependent sulfur isotope fractionation from basins included in the δ^{13}C inference. Data from different basins are separated by horizontal dashed lines; within each basin, each observation represents a unique geological unit (formation or group), plotted in stratigraphic order. The maximum and minimum age of each unit is based either on geochronological age constraints or, in cases where the unit's age is more tightly constrained by the δ^{13}C inference, on the posterior age models. Depositional age constraints are used for units that have been dated directly (e.g., formations that contain a tuff bed). The age constraints used for each unit are tabulated in Dataset S1. (*D*) Prior (i.e., geochronology-only) and posterior age range for each basin included in the inference. Basin numbers are as in panel (*C*).

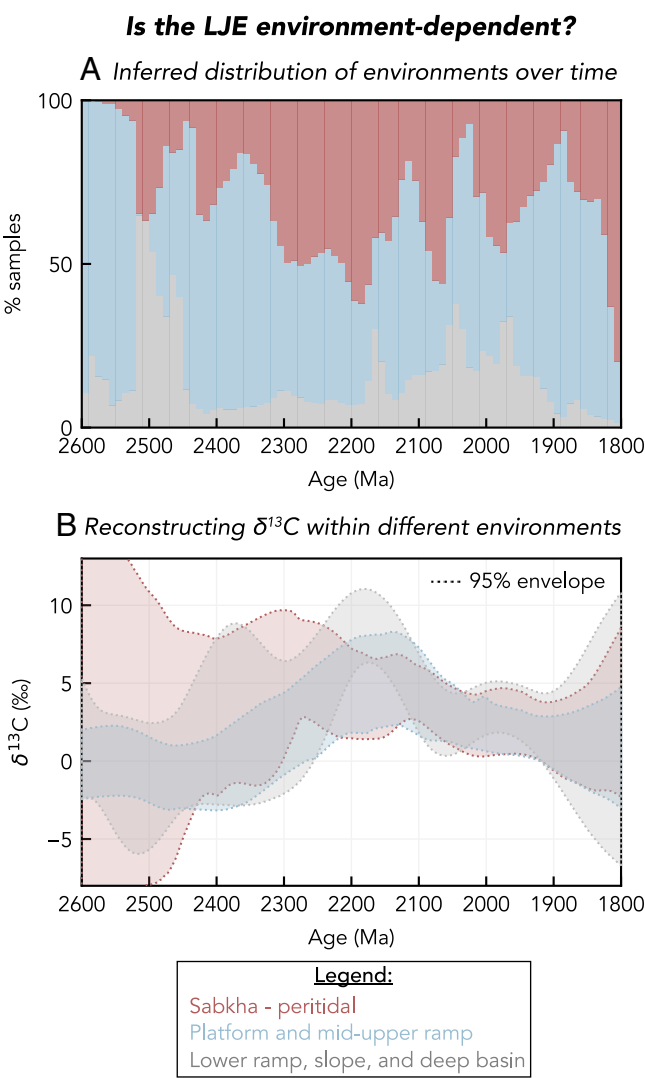**Table 1.   Lomagundi excursion summary statistics**

	Most likely	66% envelope	95% envelope
Onset (Ma)	2,445	2,462 to 2,386	2,551 to 2,238
Termination (Ma)	2,018	2,028 to 1,896	2,049 to 1,851
Duration (Myr)	429	376 to 509	211 to 624
Timing of peak (Ma)	2,130	2,302 to 2,124	2,331 to 2,107
Peak δ^{13}C value (‰)	7.3	6.1 to 8.1	5.0 to 9.5

ca. 2.3 to 2.2 Ga LJE onset, with the most likely onset occurring at 2,445 Ma (Table 1). There is only an 8% probability that the excursion onset occurs later than 2.3 Ga. This protracted early δ^{13}C rise is an important observation that aids in testing different models for the excursion. The seemingly major timing discrepancy is largely a consequence of our statistical approach, which allows for more nuanced characterization of the excursion's rising limb. The interval when δ^{13}C likely exceeds 2‰ (2,368 to 2,042 Ma; Fig. 2A) is in reasonable agreement with previous estimates for the timing of the LJE (9).

Finally, our inference omits a number of short-duration pre- and post-LJE excursions depicted in some curves (32). This departure is a consequence of fundamentally disparate assumptions about the nature of the δ^{13}C record. A standard approach to δ^{13}C reconstructions of the carbon cycle is to assume that most observed changes in δ^{13}C over time are driven by global Earth system change. Our model modifies this practice by allowing individual sections and observations to deviate from the global signal. Consequently, features that are only observed at one or a few locations (i.e., with low evidence), or that are poorly constrained in time, have limited influence on the global δ^{13}C signal inference. For example, the short-term ca. 2.0 Ga positive δ^{13}C excursion recorded by the Wooly Dolomite in Australia (45) is interpreted as a local deviation from the global signal because the majority of co-eval sections preserve near-baseline δ^{13}C values. In other cases, the posterior captures the possibility that a feature may be either global or local. For instance, in some realizations, the ca. 2.4 Ga positive excursion in the Duitschland Formation of South Africa (46) contributes to a smaller δ^{13}C maximum preceding the excursion peak at ca. 2.1 Ga; in others, it is ascribed to a local departure from near-baseline pre- or early-LJE δ^{13}C values (consistent with the interpretation of ref. 15). Similarly, data from the Great Lakes region previously have been used to argue for a brief return to baseline δ^{13}C values near 0‰ after the onset of the LJE (47). Some posterior realizations include this oscillation, but in many solutions, it is missing because the bulk of the evidence supports that global δ^{13}C values continued to rise, on average, throughout the LJE interval.

The δ^{13}C signal inference ultimately is a manifestation of evidence in the data, but the absence of short-duration δ^{13}C oscillations in our inference does not strictly preclude their existence. The model prior is designed to overlook transient (i.e., lasting only a few million years) δ^{13}C perturbations in order to detect secular change on the timescale of interest (tens of millions of years) (*Materials and Methods*). Due to the sparsity of absolute age constraints, this restriction is needed to prevent high-frequency noise from obscuring the long-term δ^{13}C signal. However, our ability to investigate shorter-term signals consequently is limited, and additional work is required to test related hypotheses.

Global Synchroneity of the LJE. The sparsity of geochronological age constraints during the Paleoproterozoic has resulted in two

Is the LJE environment-dependent?

A *Inferred distribution of environments over time*

B *Reconstructing δ^{13}C within different environments*

Legend:
Sabkha - peritidal
Platform and mid-upper ramp
Lower ramp, slope, and deep basin

Fig. 3. Environment distribution through time and environment-specific inferences. (*A*) Relative posterior abundance of samples from deep, intermediate, and shallow-water depositional environments within 10 Myr bins. Abundances are calculated using the depositional environment classification and inferred age of each sample. (*B*) Reconstructions of δ^{13}C within each depositional environment; 95% posterior envelopes mark the 2.5th and 97.5th percentiles of each inference. Note that the high uncertainty in the sabkha-peritidal inference from 2,600 to 2,400 Ma is caused by low data density.

endmember models for the LJE: the synchronous model, which adheres to the classical view that the LJE represents a single global excursion, and the asynchronous model, which postulates that the LJE instead represents multiple diachronous, shorter-duration local excursions that have been spuriously correlated. The asynchronous model has been somewhat bolstered by observations of high-δ^{13}C carbonate rocks that postdate the LJE in Australia, Fennoscandia, and Canada (35, 45, 48).

To a first order, the observation that our model infers a positive δ^{13}C excursion from the data, with no a priori knowledge of this excursion, reaffirms that the currently available observations are consistent with the synchronous model. However, this consistency should not be conflated with proof. The model is built around the assumption that a common δ^{13}C signal exists, and it favors signals that are smooth rather than very "wiggly." Consequently, the inference is predisposed toward the synchronous model: Sections with covarying δ^{13}C will be correlated unless their alignment is prohibited by geochronological age constraints,

leaving asynchronous solutions with comparatively low posterior probabilities. Thus, the situation remains largely unchanged: Given the available evidence, Occam's razor favors a synchronous LJE, but this view may be revised as new geochronological data become available. Under the synchronous model, our inference places quantitative constraints on the timing, rate, and magnitude of global $\delta^{13}C$ change.

Local Environmental Controls on Paleoproterozoic $\delta^{13}C$. Another central debate concerning the nature of the LJE is whether $\delta^{13}C$ values are controlled, or at least modulated, by depositional environment. In this view, biogeochemical cycling in restricted shallow-water (e.g., sabkha to peritidal) environments locally elevates $\delta^{13}C_{DIC}$ above contemporaneous open-ocean $\delta^{13}C_{DIC}$, which either remains near baseline values ($\sim 0‰$) or increases only moderately during the LJE (17). This hypothesis arises from the observation that the average $\delta^{13}C$ of Paleoproterozoic shallow-water carbonates is higher than that of deeper-water carbonates from the same era, and stratigraphic changes in $\delta^{13}C$ coincide with changes in depositional environment in some sections (16, 17, 25). However, evidence for environmental control remains circumstantial because low-resolution age models make it difficult to demonstrate the time-equivalence of shallow and deep-water units with distinct $\delta^{13}C$ values.

A possible mechanism for local ^{13}C enrichment has been documented in some modern restricted shallow-water environments, where methanogenesis coupled with CH_4 release to the atmosphere can elevate local $\delta^{13}C_{DIC}$ by more than $10‰$ (49, 50). Although rare today, this phenomenon may have been relatively commonplace prior to and in the immediate aftermath of the GOE when fermentation and methanogenesis were the dominant organic matter remineralization pathway (29). Photosynthesis also drives a more subdued $\delta^{13}C$ increase in both modern open-ocean surface waters and restricted shallow-water environments (51–54), providing a straightforward mechanism for minor (up to $5‰$) elevation of carbonate $\delta^{13}C$ values in productive settings.

A number of processes also can drive a local decrease in $\delta^{13}C$. For example, organic matter remineralization (55), submarine groundwater discharge (56), rapid CO_2 invasion (57), and authigenic carbonate precipitation (58) produce highly negative $\delta^{13}C$ values in some modern environments. In addition, post-depositional diagenetic alteration often lowers preserved $\delta^{13}C$ values (59, 60).

Our work suggests the LJE is a global excursion whose expression is modulated by local environmental conditions. To explicitly test for environmental controls on $\delta^{13}C$, we performed three separate inferences using observations from only deep, intermediate, or shallow-water depositional environments (Fig. 3B). These independent "within-environment" reconstructions of $\delta^{13}C$ demonstrate that all depositional environments record a large and long-lived positive excursion consistent with the LJE. While the minutia of the deep, intermediate, and shallow-water inferences differ, the fact that they overlap during most time slices supports the hypothesis that although preserved $\delta^{13}C$ values may be locally elevated or lowered—just as in today's oceans—the same common $\delta^{13}C$ signal can be found in each environment. Our results suggest that $\delta^{13}C$ may have risen earlier in shallow-water environments (Fig. 3B), but this observation should be interpreted cautiously because the pre-2.3 Ga portion of the shallow-water $\delta^{13}C$ curve is highly uncertain owing to low data

density. Minor disagreements also are expected because each inference incorporates a different subset of geochronological age constraints.

The posterior distribution of deep, intermediate, and shallow-water depositional environments over time reaffirms that the LJE is not limited to particular depositional environments (Fig. 3A). While intermediate and shallow-water samples consistently outnumber deep-water samples, all depositional environments are represented within every 10 Myr time bin between 2,500 and 1,800 Ma. The maximum abundance of shallow-water environments between 2,400 and 2,000 Ma is 62%, and the minimum abundance of deep-water environments is 6%. Importantly, however, this overrepresentation of shallow-water environments is also observed in the model prior (i.e., when sample ages are only constrained by geochronology and not by correlation of $\delta^{13}C$), where the maximum abundance of shallow-water environments is 51% and the minimum abundance of deep-water environments is 5% (*SI Appendix*, Fig. S38). If $\delta^{13}C$ were solely environment-dependent, then we would expect correlating $\delta^{13}C$ to significantly enhance the imbalance between environments in the posterior relative to the prior (i.e., alignment of $\delta^{13}C$ would lead to alignment of environments). The fact that the posterior and prior exhibit similar environmental imbalances suggests much of the bias toward shallow-water environments during the LJE can be attributed to imbalances in the data itself rather than to spurious correlation of diachronous environmental signals. In turn, these imbalances are caused by temporal changes in either the preservation potential or the primary distribution of shallow versus deep-water deposits.

While a sustained increase in global $\delta^{13}C$ is consistent with Paleoproterozoic observations, our inference requires some local modulation of preserved $\delta^{13}C$ values. Many $\delta^{13}C$ observations are offset from the inferred global signal by 1 to $5‰$ (e.g., in the Liaohe Group, China and the Lucknow Formation, South Africa), and rare samples with particularly high $\delta^{13}C$ values (e.g., in the lower Nash Fork Formation, Wyoming) sometimes deviate from the global signal by more than $10‰$. These local $\delta^{13}C$ offsets are analogous to those observed in modern carbonate sediments (49, 50, 53, 54) and compatible with previous work suggesting Paleoproterozoic $\delta^{13}C$ varies among environments (17). However, the residuals between the global signal and samples from different depositional environments do not show clear and systematic trends over time (*SI Appendix*, Fig. S39), suggesting that any environmental $\delta^{13}C$ offsets are complex and geographically variable.

Nonetheless, our inference results do imply that depositional environment exerts some influence on $\delta^{13}C$. Specifically, $\delta^{13}C$ variance both within and among different environments is greater before and during the LJE than after the excursion's termination at ca. 2.02 Ga (Figs. 2A and 3B). Amplified local $\delta^{13}C$ variance during the early Paleoproterozoic is potentially consistent with the "metabolism evolution" model for the LJE (29). This model posits that the combination of high primary productivity and methanogenesis-dominated microbial metabolism promoted high and variable $\delta^{13}C$ values following the initial rise of atmospheric O_2, with these effects waning as more energetically favorable metabolic pathways became prevalent. These biological effects on $\delta^{13}C$ would be most common in, but not strictly limited to, very shallow-water depositional environments (29). The original model offers shifting metabolic landscapes as a possible cause of the LJE, wherein the excursion is an artifact of spuriously correlating potentially asynchronous local signals. Here, we adopt

the intermediate view that the LJE is a globally synchronous excursion that was locally modulated and magnified by local biological processes. This framework explains both the extremely elevated and variable $\delta^{13}C$ values observed in some sections and the presence of a more subdued positive $\delta^{13}C$ excursion across a wide range of depositional environments (Fig. 3B).

Temporal Link Among the LJE, the GOE, and Glaciations. The LJE occurs against a backdrop of evolving atmospheric O_2 levels, major climatic upheaval, and supercraton assembly and breakup (4, 12, 26, 27). Given that the geologic carbon cycle is closely tied to each of these processes, understanding how these perturbations are related in time can help to elucidate possible cause-and-effect relationships within the broader Paleoproterozoic Earth system. Here, we leverage our inference results to interrogate temporal links among changes in $\delta^{13}C$, oxygenation, and climate.

Current geologic evidence suggests the rise of atmospheric O_2 during the GOE was oscillatory rather than unidirectional, with a gap of hundreds of millions of years between initial and permanent atmospheric oxygenation (2, 26, 27, 44, 61–63). Oscillatory O_2 levels primarily have been inferred from the repeated disappearance and reappearance of mass-independent sulfur isotope fractionation (MIF-S) in sedimentary archives (27, 64). Because MIF-S only occurs at atmospheric O_2 levels below 0.0001% of its present concentration (65), these MIF-S resurgences suggest that O_2 levels hovered near a "tipping point" during the early stages of the GOE, where close competition between oxygen sources and sinks periodically pushed atmospheric O_2 levels across the MIF-S threshold. While some MIF-S recurrences have been argued to reflect sedimentary recycling of older MIF-S signals (61, 66, 67), others have been convincingly ascribed to atmospheric O_2 oscillations (27, 44). For example, marine redox proxy data from the Transvaal Supergroup in South Africa indicate that atmospheric O_2 oscillations inferred from the MIF-S record were mirrored in the oceanic realm, providing independent evidence of surface redox instability (63). Here, we consider that the initial rise of atmospheric O_2 is marked by the earliest stratigraphic loss of MIF-S in the rock record, while permanent oxygenation is marked by the final disappearance of MIF-S.

Sulfur isotope data conservatively constrain the oscillatory O_2 interval to between 2,468 and 2,203 Ma (Fig. 2C). The oldest stratigraphic unit with no evidence of MIF-S is constrained between 2,442.2 ± 1.7 and 2,434.8 ± 6.6 Ma (42, 68), while it is very unlikely (5% probability) that any MIF-S observation is younger than 2,210 Ma. Previous estimates for the final disappearance of MIF-S are up to 114 Myr later than indicated here (2).

Accounting for all uncertainties, the inferred LJE onset either precedes or is co-eval with the oscillatory O_2 interval, and there is a 42% probability that the excursion onset predates the earliest unambiguous stratigraphic loss of MIF-S at 2,442.2 Ma (Fig. 2). This finding contrasts with previous reconstructions that suggest the LJE postdates the rise of O_2 by up to 100 Myr (10, 69). Three factors contribute to this divergence: 1) our more precise characterization of the LJE onset, which pinpoints the initiation of $\delta^{13}C$ rise rather than the first appearance of "highly elevated" $\delta^{13}C$ values, 2) variable estimates for the timing of the GOE (26, 27, 61, 70), and 3) high uncertainty in reconstructions of global $\delta^{13}C$ prior to 2.3 Ga (32). Our modeling approach addresses (3) by integrating all available $\delta^{13}C$ observations and geochronological ages within a probabilistic framework, yielding a continuous and comprehensive reconstruction of early Paleoproterozoic $\delta^{13}C$. This reconstruction hints at a more

nuanced temporal relationship between the LJE and GOE, where the initial rise of O_2 coincides with or follows the initial increase in average $\delta^{13}C$.

On the other hand, the relationship between the peak of the LJE and permanent atmospheric oxygenation is consistent with past interpretations: The final loss of MIF-S postdates the onset of the LJE and precedes the most likely LJE peak. Considering the full posterior inference, there is a 57% probability that the peak of the LJE is younger than the latest possible loss of MIF-S at 2,210 Ma. Altogether, our analysis suggests the process that caused the LJE persisted throughout the "oscillatory O_2" period, reached peak intensity after O_2 levels stabilized above 0.0001% of the present atmospheric level, and continued until $\delta^{13}C$ returned to baseline values at ca. 2.02 Ga.

These perturbations to the carbon and oxygen cycles were coeval with major climatic and environmental change. Specifically, the presence of glaciogenic diamictites at low paleolatitudes indicates the early Paleoproterozoic may have been punctuated by up to four global "snowball" glaciations (4, 71). Although the timing, number, and geographic extent of these glaciations is debated (62, 72–77), the presence of glaciogenic deposits in Africa, North America, Fennoscandia, and Australia provides strong evidence that the early Paleoproterozoic Earth was unusually susceptible to glaciation (74). Given the temporal coincidence between glaciation and O_2 oscillations, models for the GOE frequently invoke feedbacks between climate and changes in Earth's surface redox balance (64, 65, 72, 78). For instance, oxidation of atmospheric CH_4 may have triggered the collapse of a methane greenhouse, driving a rapid drop in surface temperatures that plunged Earth into a glacial state.

To investigate potential links among glaciation, the GOE, and the LJE, we use geochronological ages and the posterior section age models to constrain the age of each documented diamictite unit (SI Appendix, Fig. S40). We then use these age constraints to 1) determine which diamictites may be correlative, assuming four distinct Paleoproterozoic glacial events; and 2) compute conservative age ranges (reported as 95% probability envelopes) for each glaciation (Fig. 2B and SI Appendix).

The Paleoproterozoic glacial epoch is constrained to 2,459 to 2,214 Ma, with the oldest glaciation bracketed between 2,459 and 2,436 Ma (Fig. 2B). Evidence from Fennoscandia, where the initial MIF-S to MDF-S transition occurs stratigraphically beneath the glaciogenic Polisarka diamictite, indicates that initial oxygenation of the atmosphere precedes glaciation (61). Considering all geochronological and superposition constraints, the onset of glaciation is approximately co-eval with or up to 6 Myr younger than the earliest unambiguous loss of MIF-S and may either precede or postdate the LJE onset. The final Paleoproterozoic glaciation occurs between 2,262 and 2,214 Ma, which means the LJE onset very likely occurs prior to the termination of the glacial epoch. However, there is a 58% probability that the LJE peaks after 2,214 Ma, with the most likely peak postdating glacial termination by nearly 85 Myr. Thus, the LJE begins during a dynamic period marked by large swings in temperature and O_2 and peaks during a period of relative climate and redox stability. The wide envelopes of the early Paleoproterozoic $\delta^{13}C$ inference suggest that carbon cycling was similarly dynamic at this time, at least on local and regional scales, with $\delta^{13}C$ variability decreasing toward the end-LJE (Fig. 2A).

Implications for the Cause and Nature of the LJE. In sum, our results lend renewed confidence to the hypothesis that the LJE is a global $\delta^{13}C$ excursion that coincides with major perturbations to

both the oxygen cycle and global climate. Importantly, these conclusions are agnostic to the excursion's cause. Large-scale changes in $\delta^{13}C$ broadly reflect perturbations to the carbon cycle, but many different processes have been invoked to explain $\delta^{13}C$ excursions throughout Earth's history ([79], [80]). While the relative size of the organic matter and carbonate burial fluxes is a commonly invoked lever on $\delta^{13}C$ ([8]), models linking the LJE to other global phenomena ([18–24], [81]) are equally supported by our results. Hodgskiss et al. ([25]) provide a thorough review of competing models for the excursion. Ultimately, any explanatory model for the LJE must account for four essential features of our inference: 1) the probable duration and magnitude of the excursion ([Table 1]); 2) the rate of $\delta^{13}C$ change over time, which may provide an important constraint for coupled biogeochemical cycle models; 3) the temporal coincidence among changes in $\delta^{13}C$, atmospheric O_2 levels, and climate; and 4) the excursion's preservation in a wide range of depositional environments. As discussed previously, models invoking environmental modulation of $\delta^{13}C$ values remain compatible with—and perhaps tentatively supported by—our inference.

Limitations and Future Research Directions. The statistical approach adopted here allows us to merge fragmentary, locally variable, and time-uncertain datasets to answer the question: If the $\delta^{13}C$ values of Paleoproterozoic carbonate rocks were influenced by a global process, then what does that global signal look like? We find that this global signal is a large and long-duration positive excursion consistent with the LJE ([Fig. 2]). However, this result must be interpreted in the context of key methodological assumptions and limitations. First, due to computational limitations, our analysis only incorporates a representative subset of the existing $\delta^{13}C$ data. Our data selection algorithm maximizes spatiotemporal data coverage and ensures that stratigraphic $\delta^{13}C$ trends are optimally preserved (*Materials and Methods*). Still, some information inevitably is lost during subsampling; our approach minimizes that loss. Second, we reiterate that because the model assumes a global signal exists, it is predisposed toward the synchronous model for the LJE. Thus, while our inference is consistent with the synchronous model—meaning that the observations could be explained by the large positive $\delta^{13}C$ excursion in our posterior—it does not provide evidence against the asynchronous model. A global excursion could be spuriously inferred from sections with poor absolute age control that have been influenced by asynchronous local signals (e.g., diagenetic or environmental processes) that impart similar stratigraphic $\delta^{13}C$ patterns. Confidently distinguishing between these scenarios ultimately demands both improving the resolution of geochronological age models and constraining the processes influencing individual records via detailed sedimentological and geochemical work. Fundamentally, our approach shows what the LJE looks like if the $\delta^{13}C$ record does have a global component.

Conclusions

Our Bayesian reconstruction of Paleoproterozoic $\delta^{13}C$ suggests the LJE is a global excursion preserved in a wide range of depositional environments. The LJE very likely (95% probability) begins between 2,551 and 2,238 Ma, subsequently peaking between 2,331 and 2,107 Ma. The maximum $\delta^{13}C$ value achieved during this peak is very unlikely (5% probability) to exceed 9.1‰, with a most likely peak of 7.3‰. Investigation of the temporal relationship among the LJE, multiple sulfur isotope data, and glacial diamictite occurrences reveals that the onset of $\delta^{13}C$ rise precedes or is coeval with the earliest oxygenation of Earth's atmosphere, precedes permanent atmospheric oxygenation, and occurs before or during the Paleoproterozoic glacial epoch. The peak of the LJE likely postdates both permanent oxygenation and glaciation. The temporal coincidence among changes in $\delta^{13}C$, O_2 oscillations, and glaciation hints at—but does not require—a mechanistic link among the LJE, the GOE, and swings in climate.

More generally, our $\delta^{13}C$ inference provides an explicit framework for testing hypotheses about Paleoproterozoic carbon cycling. The timing and magnitude of $\delta^{13}C$ change, along with associated uncertainties, provide useful first-order constraints. The continuous $\delta^{13}C$ curve also can be leveraged to estimate rates of change—for example, across the rising and falling limbs of the LJE—which may help to constrain plausible drivers for the excursion. Additionally, the posterior age models can be used to place data for multiple proxy systems (e.g., C, S, U, Mo, Ca, and Mg isotopes) in the same temporal framework. This integrated approach is essential for both decoding the LJE and unraveling the broader dynamics of biogeochemical cycling on an evolving Earth.

Materials and Methods

Geochemical Data Compilation. The initial $\delta^{13}C$ database comes directly from the syn-LJE $\delta^{13}C$ compilation of Hodgskiss et al. ([25]). We modified this compilation by documenting the stratigraphic position of each sample and excluding samples interpreted as diagenetically altered by the primary source based on strong independent evidence (e.g., trace element concentrations, $\delta^{18}O$, and petrographic markers). We then expanded the database to include recently published data and data from formations that pre- and postdate the LJE. All $\delta^{13}C$ values are recorded with analytical uncertainty; if the uncertainty was not reported by the primary source, we assume a value of ± 0.2‰ (1σ). The complete $\delta^{13}C$ database is provided in [Dataset S1].

Geochronological Age Constraints. The age of each stratigraphic section is constrained by depositional and/or limiting (detrital and intrusive) geochronological ages. All ages are recorded with the uncertainty reported in the primary source; since the inference model integrates dates from multiple decay systems, we use uncertainties that include decay constant errors when available. Sections that are missing a minimum or maximum age constraint but that are confidently mapped as Paleoproterozoic are assigned a nominal minimum/maximum age of 1,600 or 2,500 $\pm$ 50 Ma, respectively. Where necessary, we manually stack sections from different sources to encode known superposition relationships (e.g., constrained by regional mapping of geological formations) that are not strictly enforced by geochronological constraints.

In most cases, all informative geochronological ages are included in the model. In rare cases where ages violate superposition, we select the age that is reproducible (corroborated by multiple independent sources) or that is more reliable, based on both our own and previous authors' assessment of the data. For example, we consider that whole-rock carbonate U-Pb system dates typically are less reliable than igneous zircon U-Pb system dates, as evidenced by typically higher uncertainties and mean squared weighted deviation (MSWD) values. When considering detrital mineral ages, we only consider "youngest single grain" ages if the age of at least one additional grain overlaps within 2σ uncertainty. *SI Appendix*, Figs. S4–S36 show the age constraints used for each basin; where appropriate, we discuss specific age constraint choices in *SI Appendix*. In total, 124 unique age constraints are included in the inference.

Data Subsampling. We subsampled the $\delta^{13}C$ data because the model's computational complexity scales as $\mathcal{O}(n^3)$, where n is the number of observations ([82]). Consequently, inference is intractable for more than several hundred $\delta^{13}C$ observations.

To subsample the data, we first assigned each stratigraphic section to a priority level between one (high priority) and four (low priority) using criteria that promote wide geographic and temporal coverage and deprioritize redundant (e.g., duplicate sections through the same formation) or potentially unreliable (e.g., sections with poor or missing age constraints) data. Criteria and priority level assignments are tabulated in *SI Appendix*. All sections assigned to priority levels one and two ($N = 76$) are included in the inference, while lower-priority sections are excluded.

Then, we subsampled each section such that the overall stratigraphic trends are retained while redundant data and noise are removed. The section subsampling procedure (*SI Appendix*, Fig. S2) retains the minimum number of data points required to achieve a subsampled stratigraphic signal that is sufficiently similar to the full-resolution signal. The subsampled dataset contains 849 δ^{13}C observations from sections with priority levels one and two, compared to 4,825 prior to subsampling. Both the original and subsampled data for each basin are shown in *SI Appendix*, Figs. S4–S36.

Paleoproterozoic δ^{13}C Inference. Essential aspects of our Bayesian statistical model are summarized in the main text, and the model is extensively described and tested in Edmonsond and Dyer (36). The model is available as an open-source Python package, StratMC (https://stratmc.readthedocs.io/) (83), which is built on the probabilistic programming package PyMC (84). Here, we expand on the model structure and detail the parameters used to reconstruct Paleoproterozoic δ^{13}C.

The prior age model for each section encompasses depositional histories ranging from continuous to highly episodic. We assume only that sample ages decrease upsection (stratigraphic superposition) and that the age of each sample must respect superposition with any over- and underlying geochronological age constraints. All geochronological ages are modeled as normal distributions with mean and SD equal to the reported age and its uncertainty. Geochronological ages that directly date a given δ^{13}C observation (e.g., carbonate Pb-Pb dates), rather than providing a minimum or maximum constraint on its age, are enforced via a term in the model likelihood function.

The shared (global) δ^{13}C signal as a function of time, $f(t)$, is modeled as a Gaussian process (GP). A GP defines a distribution of random functions described by their mean, $m(t)$, and covariance, $k(t, t')$ (82):

$$f(t) \sim GP(m(t), k(t, t')) \qquad [1]$$

We set the GP covariance function to the sum of a radial basis function (RBF) kernel and a white noise kernel with variance equal to 0.1. The GP mean function is a constant, and its prior is a normal distribution with μ and σ equal to the mean and SD of the δ^{13}C observations.

The prior for the RBF kernel lengthscale is attuned to detect δ^{13}C oscillations on the timescale of interest. Since we aim to reconstruct sustained changes in δ^{13}C across the LJE, which has a minimum duration of 128 Myr (9), we define the lengthscale prior such that changes in δ^{13}C occurring on significantly shorter timescales are ignored. Specifically, the lengthscale prior is a Wald distribution with $\mu = 25$ and $\lambda = 50$ that has been translated by $+60$. Restricting the prior lengthscale is necessary to ensure the long-term δ^{13}C trend is not masked by higher-frequency variability.

Previous observations suggest the δ^{13}C values recorded by any given stratigraphic section may be influenced by local processes (e.g., local carbon cycling and diagenesis) that are unrelated to the global signal (34). To capture this expectation, the δ^{13}C value of each sample is modeled as a normal distribution with a mean equal to the sum of the GP evaluated at the sample age and a per-section offset term (ϕ_{section}), and SD equal to the sum of measurement uncertainty (σ_{sample}) and a per-section geologic noise term (η_{section}):

$$\delta^{13}C_{\text{sample}} \sim Normal(f(t) + \phi_{\text{section}}, \sigma_{\text{sample}} + \eta_{\text{section}}) \qquad [2]$$

The per-section offset priors are Laplace distributions with $\mu = 0$ and $b = 2$, while the per-section geologic noise priors are half-Cauchy (positive only) distributions with $\beta = 1$. Both of these distributions assign the highest prior probability to solutions with no local deviations from the global signal but have fat tails (high kurtosis) that allow for a wide range of offset and noise values.

The posterior distributions are sampled using the No-U-Turn Sampler (85) implemented in PyMC (84). The model posterior is sampled by at least 100 independent Markov chains. Each simulation is run for 3,000 steps, with the first 2,000 samples used for tuning (sampler "burn-in") and then discarded. Convergence is evaluated using criteria detailed in *SI Appendix*.

1. J. Farquhar, H. Bao, M. Thiemens, Atmospheric influence of Earth's earliest sulfur cycle. *Science* **289**, 756–758 (2000).
2. M. S. W. Hodgskiss, E. A. Sperling, A prolonged, two-step oxygenation of Earth's early atmosphere: Support from confidence intervals. *Geology* **50**, 158–162 (2021).
3. H. D. Holland, Volcanic gases, black smokers, and the Great Oxidation Event. *Geochim. Cosmochim. Acta* **66**, 3811–3826 (2002).
4. D. A. Evans, N. J. Beukes, J. L. Kirschvink, Low-latitude glaciation in the Palaeoproterozoic era. *Nature* **386**, 262–266 (1997).
5. L. R. Kump, M. E. Barley, Increased subaerial volcanism and the rise of atmospheric oxygen 2.5 billion years ago. *Nature* **448**, 1033–1036 (2007).
6. A. H. Knoll, M. A. Nowak, The timetable of evolution. *Sci. Adv.* **3**, e1603076 (2017).
7. I. N. Bindeman *et al.*, Rapid emergence of subaerial landmasses and onset of a modern hydrologic cycle 2.5 billion years ago. *Nature* **557**, 545–548 (2018).
8. J. A. Karhu, H. D. Holland, Carbon isotopes and the rise of atmospheric oxygen. *Geology* **24**, 867–870 (1996).
9. A. P. Martin, D. J. Condon, A. R. Prave, A. Lepland, A review of temporal constraints for the Paleoproterozoic large, positive carbonate carbon isotope excursion (the Lomagundi-Jatuli Event). *Earth Sci. Rev.* **127**, 242–261 (2013).
10. A. Bekker, H. Holland, Oxygen overshoot and recovery during the early Paleoproterozoic. *Earth Planet. Sci. Lett.* **317–318**, 295–304 (2012).
11. V. A. Melezhik, A. E. Fallick, P. V. Medvedev, V. V. Makarikhin, Extreme ^{13}C$_{\text{carb}}$ enrichment in ca. 2.0 Ga magnesite-stromatolite-dolomite-'red beds' association in a global context: A case for the world-wide signal enhanced by a local environment. *Earth Sci. Rev.* **48**, 71–120 (1999).
12. A. Bekker, J. Karhu, K. Eriksson, A. Kaufman, Chemostratigraphy of Paleoproterozoic carbonate successions of the Wyoming Craton: Tectonic forcing of biogeochemical change? *Precambr. Res.* **120**, 279–325 (2003).
13. P. Aharon, Redox stratification and anoxia of the early Precambrian oceans: Implications for carbon isotope excursions and oxidation events. *Precambr. Res.* **137**, 207–222 (2005).
14. J. M. Hayes, J. R. Waldbauer, The carbon cycle and associated redox processes through time. *Philos. Trans. R. Soc. B Biol. Sci.* **361**, 931–950 (2006).
15. F. Frauenstein, J. Veizer, N. Beukes, H. Van Niekerk, L. Coetzee, Transvaal Supergroup carbonates: Implications for Paleoproterozoic δ^{18}O and δ^{13}C records. *Precambr. Res.* **175**, 149–160 (2009).
16. K. B. Mayika *et al.*, The Paleoproterozoic Francevillian succession of Gabon and the Lomagundi-Jatuli event. *Geology* **48**, 1099–1104 (2020).
17. A. Prave *et al.*, The grandest of them all: The Lomagundi-Jatuli Event and Earth's oxygenation. *J. Geol. Soc.* **179**, jgs2021-036 (2022).
18. G. A. Shields, B. J. W. Mills, Tectonic controls on the long-term carbon isotope mass balance. *Proc. Natl. Acad. Sci. U.S.A.* **114**, 4318–4323 (2017).
19. Y. Miyazaki, N. J. Planavsky, E. W. Bolton, C. T. Reinhard, Making sense of massive carbon isotope excursions with an inverse carbon cycle model. *J. Geophys. Res. Biogeosci.* **123**, 2485–2496 (2018).
20. J. Eguchi, J. Seales, R. Dasgupta, Great Oxidation and Lomagundi events linked by deep cycling and enhanced degassing of carbon. *Nat. Geosci.* **13**, 71–76 (2020).
21. J. Eguchi, C. W. Diamond, T. W. Lyons, Proterozoic supercontinent break-up as a driver for oxygenation events and subsequent carbon isotope excursions. *PNAS Nexus* **1**, 2 (2022).
22. J. Higgins, W. Fischer, D. Schrag, Oxygenation of the ocean and sediments: Consequences for the seafloor carbonate factory. *Earth Planet. Sci. Lett.* **284**, 25–33 (2009).
23. D. P. Schrag, J. A. Higgins, F. A. Macdonald, D. T. Johnston, Authigenic carbonate and the history of the global carbon cycle. *Science* **339**, 540–543 (2013).
24. T. A. Laakso, D. P. Schrag, *Isotopic Constraints on Earth System Processes*, K. Sims, K. Maher, D. P. Schrag, Eds. (Wiley & Sons, Hoboken, NJ, 2022), pp. 205–216.
25. M. S. Hodgskiss, P. W. Crockford, A. V. Turchyn, Deconstructing the Lomagundi-Jatuli carbon isotope excursion. *Annu. Rev. Earth Planet. Sci.* **51**, 301–330 (2023).
26. A. P. Gumsley *et al.*, Timing and tempo of the Great Oxidation Event. *Proc. Natl. Acad. Sci. U.S.A.* **114**, 1811–1816 (2017).

27. S. W. Poulton et al., A 200-million-year delay in permanent atmospheric oxygenation. Nature 592, 232–236 (2021).

28. R. R. Large et al., Evidence that the GOE was a prolonged event with a peak around 1900 Ma. Geosyst. Geoenviron. 1, 100036 (2022).

29. D. Y. Sumner, Oxygenation of Earth's atmosphere induced metabolic and ecologic transformations recorded in the Lomagundi-Jatuli carbon isotopic excursion. Appl. Environ. Microbiol. 90, e00093–24 (2024).

30. V. A. Melezhik et al., 7.3 The Palaeoproterozoic Perturbation of the Global Carbon Cycle: The Lomagundi-Jatuli Isotopic Event, V. A. Melezhik et al., Eds. (Springer, Berlin Heidelberg, Berlin, Heidelberg, 2013), pp. 1111–1150.

31. T. W. Lyons, C. T. Reinhard, N. J. Planavsky, The rise of oxygen in Earth's early ocean and atmosphere. Nature 506, 307–315 (2014).

32. A. Bekker, Lomagundi Carbon Isotope Excursion, M. Gargaud et al., Eds. (Springer Berlin Heidelberg, Berlin, Heidelberg, 2022), pp. 1–7.

33. P. M. Sadler, Sediment accumulation rates and the completeness of stratigraphic sections. J. Geol. 89, 569–584 (1981).

34. A. S. Ahm, J. Husson, Local and Global Controls on Carbon Isotope Chemostratigraphy, Elements in Geochemical Tracers in Earth System Science (Cambridge University Press, 2022).

35. A. Martin et al., Multiple Palaeoproterozoic carbon burial episodes and excursions. Earth Planet. Sci. Lett. 424, 226–236 (2015).

36. S. Edmonsond, B. Dyer, A Bayesian framework for inferring regional and global change from stratigraphic proxy records (StratMC v1.0). Geosci. Model Dev. 18, 4759–4788 (2025).

37. S. E. Peters, J. M. Husson, J. Czaplewski, Macrostrat: A platform for geological data integration and deep-time Earth crust research. Geochem. Geophys. Geosyst. 19, 1393–1409 (2018).

38. V. A. Melezhik, A. E. Fallick, A. B. Kuznetsov, Palaeoproterozoic, rift-related,, ^{13}C-rich, lacustrine carbonates, NW Russia. Part II: Global isotope signal recorded in the lacustrine dolostones. Earth Environ. Sci. Trans. R. Soc. Edinb. 95, 423–444 (2005).

39. V. A. Melezhik, H. Huhma, D. J. Condon, A. E. Fallick, M. J. Whitehouse, Temporal constraints on the Palaeoproterozoic Lomagundi-Jatuli carbon isotopic event. Geology 35, 655–658 (2007).

40. A. Martin et al., Dating the termination of the Palaeoproterozoic Lomagundi-Jatuli carbon isotopic event in the North Transfennoscandian Greenstone Belt. Precambr. Res. 224, 160–168 (2013).

41. P. E. Salminen, J. A. Karhu, V. A. Melezhik, Kolosjoki sedimentary formation: A record in the aftermath of the Palaeoproterozoic global positive δ^{13}C excursion in sedimentary carbonates. Chem. Geol. 362, 165–180 (2013).

42. Y. Amelin, L. Heaman, V. Semenov, U-Pb geochronology of layered mafic intrusions in the eastern Baltic Shield: Implications for the timing and duration of Paleoproterozoic continental rifting. Precambr. Res. 75, 31–46 (1995).

43. V. Selvaraja, S. Caruso, M. Fiorentini, C. LaFlamme, The global sedimentary sulfur isotope database (The Centre for Exploration Targeting, University of Western Australia, 2019). https://doi.org/10.26182/12r5-6z79. Accessed 1 March 2025.

44. B. T. Uveges, G. Izon, S. Ono, N. J. Beukes, R. E. Summons, Reconciling discrepant minor sulfur isotope records of the Great Oxidation Event. Nat. Commun. 14, 279 (2023).

45. A. Bekker, B. Krapež, S. G. Müller, J. A. Karhu, A short-term, post-Lomagundi positive C isotope excursion at c. 2.03 Ga recorded by the Wooly Dolomite, Western Australia. J. Geol. Soc. 173, 689–700 (2016).

46. A. Bekker et al., Chemostratigraphy of the Paleoproterozoic Duitschland Formation, South Africa: Implications for coupled climate change and carbon cycling. Am. J. Sci. 301, 261–285 (2001).

47. A. Bekker, J. Karhu, A. Kaufman, Carbon isotope record for the onset of the Lomagundi carbon isotope excursion in the Great Lakes area. North Am. Precambr. Res. 148, 145–180 (2006).

48. H. J. Hofmann, A. Davidson, Paleoproterozoic stromatolites, Hurwitz Group, Quartzite Lake area, Northwest Territories, Canada. Can. J. Earth Sci. 35, 280–289 (1998).

49. D. Birgel et al., Methanogenesis produces strong ^{13}C enrichment in stromatolites of Lagoa Salgada, Brazil: A modern analogue for Palaeo-/Neoproterozoic stromatolites?. Geobiology 13, 245–266 (2015).

50. P. Cadeau et al., Carbon isotope evidence for large methane emissions to the proterozoic atmosphere. Sci. Rep. 10, 18186 (2020).

51. P. Kroopnick, The distribution of δ^{13}C of ΣCO$_2$ in the world oceans. Deep Sea Res. Part A. Oceanogr. Res. Pap. 32, 57–84 (1985).

52. J. Lynch-Stieglitz, T. F. Stocker, W. S. Broecker, R. G. Fairbanks, The influence of air-sea exchange on the isotopic composition of oceanic carbon: Observations and modeling. Glob. Biogeochem. Cycles 9, 653–665 (1995).

53. E. C. Geyman, A. C. Maloof, A diurnal carbon engine explains δ^{13}C-enriched carbonates without increasing the global production of oxygen. Proc. Natl. Acad. Sci. U.S.A. 116, 24433–24439 (2019).

54. E. J. Trower et al., Revisiting elevated delta^{13}C values of sediment on modern carbonate platforms. Geophys. Res. Lett. 51, e2023GL107703 (2024).

55. C. L. Pederson et al., Seawater chemistry of a modern subtropical 'epeiric' sea: Spatial variability and effects of organic decomposition. Geochim. Cosmochim. Acta 314, 159–177 (2021).

56. W. P. Patterson, L. M. Walter, Depletion of δ^{13}C in seawater ΣCO$_2$ on modern carbonate platforms: Significance for the carbon isotopic record of carbonates. Geology 22, 885–888 (1994).

57. I. D. Clark, J. C. Fontes, P. Fritz, Stable isotope disequilibria in travertine from high pH waters: Laboratory investigations and field observations from Oman. Geochim. Cosmochim. Acta 56, 2041–2050 (1992).

58. T. H. Naehr et al., Authigenic carbonate formation at hydrocarbon seeps in continental margin sediments: A comparative study. Deep Sea Res. Part II Top. Stud. Oceanogr. 54, 1268–1291 (2007).

59. J. Allan, R. Matthews, Isotope signatures associated with early meteoric diagenesis. Sedimentology 29, 797–817 (1982).

60. J. Higgins et al., Mineralogy, early marine diagenesis, and the chemistry of shallow-water carbonate sediments. Geochim. Cosmochim. Acta 220, 512–534 (2018).

61. M. R. Warke et al., The great oxidation event preceded a Paleoproterozoic "snowball Earth". Proc. Natl. Acad. Sci. U.S.A. 117, 13314–13320 (2020).

62. A. E. Millikin et al., A new Re-Os age constraint informs the dynamics of the Great Oxidation Event. Geology 52, 857–862 (2024).

63. C. M. Ostrander et al., Onset of coupled atmosphere-ocean oxygenation 2.3 billion years ago. Nature 631, 335–339 (2024).

64. D. G. Ruiz, C. Goldblatt, A. S. Ahm, Climate variability leads to multiple oxygenation episodes across the Great Oxidation Event. Geophys. Res. Lett. 51, e2023GL106694 (2024).

65. K. Zahnle, M. Claire, D. Catling, The loss of mass-independent fractionation in sulfur due to a Palaeoproterozoic collapse of atmospheric methane. Geobiology 4, 271–283 (2006).

66. C. T. Reinhard, N. J. Planavsky, T. W. Lyons, Long-term sedimentary recycling of rare sulphur isotope anomalies. Nature 497, 100–103 (2013).

67. P. Philippot et al., Globally asynchronous sulphur isotope signals require re-definition of the Great Oxidation Event. Nat. Commun. 9, 2245 (2018).

68. A. Brasier et al., Earth's earliest global glaciation? Carbonate geochemistry and geochronology of the Polisarka Sedimentary Formation. Kola Peninsula. Russia. Precambr. Res. 235, 278–294 (2013).

69. K. O. Konhauser et al., Aerobic bacterial pyrite oxidation and acid rock drainage during the Great Oxidation Event. Nature 478, 369–373 (2011).

70. G. Luo et al., Rapid oxygenation of Earth's atmosphere 2.33 billion years ago. Sci. Adv. 2, e1600134 (2016).

71. J. L. Kirschvink et al., Paleoproterozoic snowball Earth: Extreme climatic and geochemical global change and its biological consequences. Proc. Natl. Acad. Sci. U.S.A. 97, 1400–1405 (2000).

72. R. E. Kopp, J. L. Kirschvink, I. A. Hilburn, C. Z. Nash, The Paleoproterozoic snowball Earth: A climate disaster triggered by the evolution of oxygenic photosynthesis. Proc. Natl. Acad. Sci. U.S.A. 102, 11131–11136 (2005).

73. B. Rasmussen, A. Bekker, I. R. Fletcher, Correlation of Paleoproterozoic glaciations based on U-Pb zircon ages for tuff beds in the Transvaal and Huronian Supergroups. Earth Planet. Sci. Lett. 382, 173–180 (2013).

74. G. M. Young, Contradictory correlations of Paleoproterozoic glacial deposits: Local, regional or global controls? Precambr. Res. 247, 33–44 (2014).

75. A. Bekker, B. Krapež, J. A. Karhu, Correlation of the stratigraphic cover of the Pilbara and Kaapvaal cratons recording the lead up to Paleoproterozoic Icehouse and the GOE. Earth Sci. Rev. 211, 103389 (2020).

76. P. Philippot et al., Comment on "Correlation of the stratigraphic cover of the Pilbara and Kaapvaal cratons recording the lead up to Paleoproterozoic Icehouse and the GOE" by Andrey Bekker, Bryan Krapež, and Juha A. Karhu, 2020, Earth Science Reviews, https://doi.org/10.1016/j.earscirev.2020.103389. Earth Sci. Rev. 218, 103594 (2021).

77. B. Rasmussen, J. Wei Zi, A. Bekker, New U-Pb zircon tuff ages and revised stratigraphic correlations in the Superior craton during the Great Oxidation Episode. Earth Planet. Sci. Lett. 640, 118779 (2024).

78. A. A. Pavlov, J. F. Kasting, L. L. Brown, K. A. Rages, R. Freedman, Greenhouse warming by CH$_4$ in the atmosphere of early Earth. J. Geophys. Res. Planets 105, 11981–11990 (2000).

79. L. R. Kump, M. A. Arthur, Interpreting carbon-isotope excursions: Carbonates and organic matter. Chem. Geol. 161, 181–198 (1999).

80. B. Cramer, I. Jarvis, "Chapter 11 - carbon isotope stratigraphy" in Geologic Time Scale 2020, F. M. Gradstein, J. G. Ogg, M. D. Schmitz, G. M. Ogg, Eds. (Elsevier, 2020), pp. 309–343.

81. A. Bachan, L. R. Kump, The rise of oxygen and siderite oxidation during the Lomagundi Event. Proc. Natl. Acad. Sci. U.S.A. 112, 6562–6567 (2015).

82. C. E. Rasmussen, C. K. Williams et al., Gaussian Processes for Machine Learning (MIT Press, 2006).

83. S. Edmonsond, StratMC v1.0.0. Zenodo. https://doi.org/10.5281/zenodo.13281935. Deposited 8 April 2025.

84. O. Abril-Pla et al., PyMC: A modern and comprehensive probabilistic programming framework in Python. PeerJ Comput. Sci. 9, e1516 (2023).

85. M. D. Hoffman, A. Gelman, The no-u-turn sampler: Adaptively setting path lengths in Hamiltonian Monte Carlo. J. Mach. Learn. Res. 15, 1593–1623 (2014).

86. S. Edmonsond, Data and code for "Timing and magnitude of the Lomagundi-Jatuli carbon isotope excursion." Zenodo. https://doi.org/10.5281/zenodo.15460760. Deposited 19 May 2025.